

Textural and Catalytic Properties of Combinational Micro-Mesoporous Octatitanate Fibers Prepared by Solvothermal Soft Chemical Process

Ningzhong Bao,* Liming Shen, and Kazumichi Yanagisawa

Research Laboratory of Hydrothermal Chemistry, Faculty of Science, Kochi University, Kochi 780-8520, Japan

Received: July 14, 2004; In Final Form: August 24, 2004

Protonic octatitanate fibers with novel combinational micro-mesoporous structures were prepared by using solvothermal soft chemical process in glycerine. Potassium titanate of $K_2Ti_4O_9$, which has a fibrous morphology and microstructures organized with K_2O -rich melt on mesoscale, was used as a precursor. In the first step, the potassium titanate precursor was treated with an acidic solution to obtain layered protonic tetratitanate. In the second step, the layered protonic tetratitanate was treated in glycerine under mild conditions to transfer the layered structure to the tunnel-like structure of protonic octatitanate fibers. Textural and catalytic properties of the protonic octatitanate fibers were investigated. They are fibers (0.5–1.5 μm in diameter and 10–20 μm in length) consisting of nanowhiskers with the average diameter of around 30 nm. The nanowhiskers further consist of microporous nanorods (around 3 nm in diameter and 5–10 nm in lengths) and nanoslits (1–2 nm in width and up to 8 nm in length). In addition, mesopores with diameters in main ranges of 1–4 and 20–40 nm exist within the octatitanate fibers. The solvothermally treated octatitanate fibers exhibit highly photocatalytic activity for the photodegradation of methyl orange. The interfacial charge transfer is also quickened because of a large amount of surface active sites and adsorbed reactants of O_2 , hydroxyl OH, glycerine, and methyl orange. The number and strength of surface acid sites on the octatitanate fibers were measured quantitatively by the technique of microcalorimetric adsorption, using ammonia as the probe molecule. The octatitanate fibers prepared by thermal treatment in air exhibit the very strong acidity with an initial heat of 145 kJ/mol and coverage of 1100 $\mu\text{mol/g}$ for the adsorption of NH_3 , showing potential application in solid acid catalysis.

1. Introduction

TiO_2 -based materials have been widely studied in both solid acid catalysis¹ and photocatalysis,² and their catalytic activities are mainly determined by crystallinity and surface area.^{3–7} For the influence of crystallinity on the materials catalytic activities, most amorphous polymorphs are nonfeasible for many catalytic reactions³, and many low-crystallinity photocatalysts have low catalytic activities because the defect generally existing in the low-crystalline materials works as recombination sites between photogenerated electrons and holes.⁴ Therefore, materials with better crystallinity and fewer defects often are active catalysts.⁵ For the influence of surface area on the materials catalytic activities, to create a larger surface area helps to improve the catalytic activity of materials because most catalytic reactions occur on the catalyst surface and a large surface increases the amount of surface active sites.⁶ As a result, for TiO_2 -based materials with both high crystallinity and large surface area, they are indispensable for efficient and propagable catalytic applications. Two effective strategies, described below, have been developed to prepare materials with good crystallinity and large surface area.

One strategy is to prepare nanocrystals by using various methods such as microemulsion,⁷ CVD,⁸ nonhydrolytic solution method,⁹ sol–gel method,¹⁰ and so on. The prepared nanocrystals have both high crystallinity and large surface area.¹¹ However, most synthesis methods are of high cost for production and low yield for products, and the nanocrystals are hard to

recover for reuse, too.¹² The technology of large supports for reuse¹³ lowers the surface area-to-volume of catalysts, decreasing the amount of active surface sites of catalysts, inducing the difference for the interfacial structure or mass-transfer limitations, and lowering the use ratio of light.^{14–16} Therefore, additional technologies and novel designs for reactors are required in order to overcome these disadvantages. For example, the light use ratio was increased from the lowest 10% to the highest 95% in a developed and optimized TiO_2 -coated fiber-optic cable reactor, resulting in maximum quantum efficiency comparable to a TiO_2 slurry reactor operated under similar conditions.^{17,18}

Another strategy is to produce nanoporous materials that have received great scientific and technological interest because of their strong abilities to interact with ions, atoms, and molecules not only on the outer surface but also throughout the whole bulk materials.^{6,19–20} For nanoporous materials, solids of zeolites have three-dimensional crystalline frameworks and interpenetrating micropore channels (<10 Å in diameter). However, the small micropores of zeolites cannot allow the fixation of large active complexes, the reduction of the diffusion restriction of reactants, and reactions involving bulky molecules.^{6,19–21} Although a wide range of mesoporous materials with main pore diameters of 2–50 nm were synthesized by attractive surfactant-mediated synthesis methods,^{6,19–20} the majority of ordered mesoporous materials cannot be synthesized in crystalline form, and only several limited low-ordered with semicrystalline or relatively high crystalline mesoporous materials have been reported.^{22–25} Therefore, how to prepare crystalline materials with both micropores and mesopores presents a challenge.

* Corresponding author. Fax: 81-88-844-8362. E-mail: nzh_bao@yahoo.com.

TABLE 1: Chemical Component and Material Characteristics of Samples

sample	components	synthesis condition		BET surface area (m ² g ⁻¹)	a	b	pore volume (cm ³ g ⁻¹)
		media	T (°C)				
A	K ₂ Ti ₄ O ₉	air	1000	5.6	0.0	—	—
B	H ₂ Ti ₄ O ₉ ·1.2H ₂ O	air	60	119.0	90.3	1–4, 20–40	0.046
C	(H ₃ O) _{0.5} H _{1.5} Ti ₈ O ₁₇ ·H ₂ O	air	250	100.5	70.2	1–4, 20–40	0.042
D	(H ₃ O) _{0.5} H _{1.5} Ti ₈ O ₁₇ ·H ₂ O	glycerine	250	127.2	79.3	1–4, 20–40	0.051
P-25	anatase(70%), rutile(30%)	—	—	50.23	—	—	—

^a Surface area (m² g⁻¹) of micropores (<1 nm) calculated by the MP-method. ^b Main diameter distributions of mesopores calculated from N₂ desorption isotherms by the BJH method.

It has been reported that layered alkali metal or protonic titanates are excellent precursors that were used to prepare many TiO₂-based materials, with various morphologies, phase types, and crystallinities,^{26–42} showing potential applications in photocatalysis^{27–29} and solid acid catalysis.^{30–31} When replacing crystalline titania reactants with amorphous titania, potassium titanates with controlled microstructures, chemical compositions and crystallinities were prepared under a mild and continuous calcination.^{32–35} Many types of fibrous titanates and titania with large micron sizes that can be easily separated from solution through simple sedimentation in short time were prepared by ion exchange reaction and soft chemical routes.^{26–42} Further, the hydrothermal and solvothermal soft chemical process is a useful method for controlling crystallinity, structure, and chemical composition of layered titanates.^{29,37} In the present study, we describe the preparation of the protonic octatitanate fibers with novel combinational micro-mesoporous structure and enhanced catalytic activities by using solvothermal soft chemical process, and we discuss the reason of their enhanced catalytic activities both in photocatalysis and in solid acid catalysis. Degussa P-25 and methyl orange were used as a standard sample and as a model pollutant in photocatalysis study, respectively. Microcalorimetric measurements for the adsorption of NH₃ were conducted to quantitatively measure the number and strength of surface acid sites on the octatitanate fibers. The obtained titanate fibers are of novel combinational micro-mesoporous structure and new catalytic properties that may be useful for extending the application of titanates in photocatalysis and for solid acid catalysis.

2. Experimental Section

Potassium tetratitanate fibers (K₂Ti₄O₉), designated “A”, were prepared by calcination of the mixture of amorphous titania hydrate and K₂CO₃ with TiO₂/K₂O molar ratio of 3.0 at 1000 °C for 2 h. Layered protonic tetratitanate fibers (H₂Ti₄O₉·1.2H₂O), designated “B”, were then prepared by the ion exchange of K₂Ti₄O₉ fibers in acidic solution at pH <1.0. The protonic octatitanate fibers ((H₃O)_{0.5}H_{1.5}Ti₈O₁₇·H₂O), designated “C” and “D”, were prepared from the layered protonic H₂Ti₄O₉·1.2H₂O fibers by thermal treatments in air at 250 °C for 24 h and in glycerin at 250 °C for 24 h, respectively. They were washed with alcohol and finally dried at 60 °C in a vacuum for 24 h.

X-ray diffraction (XRD) patterns of samples were obtained on a Bruker D8 Advance X-ray diffractometer (Cu Kα₁ irradiation, λ = 1.5406 Å), in the continuous scan mode at 5 ~ 80 °(2θ) with a scanning rate of 0.02 °(2θ)/second. The surface area and pore size distribution of samples were determined by the amount of N₂ adsorption at 77 K. A Coulter Ominisorb 11CX, USA, was employed to obtain adsorption/desorption isotherms. The specific surface area was calculated in a relative pressure range of 0.05 < P/P₀ < 0.2. MP method, an extension of T-plot procedure, was used to calculate the micropore volume

and micropore surface. BJH method was used to evaluate the mesopores. FT-IR spectra were recorded on pellets of the samples mixed with KBr on a Bruker IFS666V FT-IR spectrometer in the range of 400–4000 cm⁻¹ at a resolution of 2 cm⁻¹. The mass content of potassium in samples was measured by atomic adsorption spectroscope (WFX-10, Beijing Ruili Analysis Instrument Co. Ltd., P. R. China). Morphologies and microstructures of samples were observed by scanning electron microscope (SEM, JSM-6300, Japan) and high-resolution transmission electron microscope (HRTEM, JEM2010, Japan).

Photocatalytic reaction was carried out on stirred suspensions at 25 °C in a 1.5 L Pyrex reactor. Methyl orange was dissolved in suspensions containing the prepared catalysts. The 1 L solution containing 20 mg·L⁻¹ of methyl orange and 0.5 g·L⁻¹ of catalyst was air equilibrated and stirred at 800 rpm for 10 min before irradiation by a 300 W Hg lamp. The solutions were prepared with deionized water and reagent-grade chemicals. The pH value of reaction solution was maintained at 3.0 by adding concentrated HNO₃ solution. Because the total added volume of acid solution is less than 10 mL, this volume influence on the concentration variation of chemicals was omitted. A small amount of reaction solutions was taken intermittently for analysis. The methyl orange concentrations were then determined by an UV spectrophotometer. Degussa P-25, one standard sample in photocatalysis study, was used to evaluate photocatalytic activities of our samples.

Microcalorimetric measurements for the adsorption of NH₃ were carried out using a Tian-Calvet heat-flux apparatus reported.^{43,44} The microcalorimeter was connected to a gas-handling and volumetric adsorption system, equipped with a Baratron capacitance manometer (MKS) for precision pressure measurement. The differential heat of adsorption versus adsorbate coverage was obtained by measuring the heats evolved when doses of a gas (2–5 μmol) were admitted sequentially onto the catalyst until the surface was saturated by the adsorbate. Ammonia with a purity of 99.99% was used. Before microcalorimetric measurements, samples were typically dried under vacuum at 150 °C for 1 h. Microcalorimetric adsorptions of ammonia were performed at 150 °C.

3. Results and Discussion

3.1. Textural and Surface Properties of Combinational Micro-Mesoporous Titanate Fibers. The textural and surface properties are key factors that influence both the activity of catalysts and the efficiency of catalytic reactions. In the present study, novel combinational micro-mesoporous titanate fibers with both larger surface area and good crystallinity were prepared by employing soft chemical routes of ion exchange and thermal treatments. The preparation conditions, chemical components, surface areas, and pore structural characteristics of samples A to D and P-25 are shown in Table 1. Potassium mass contents for sample B–D are all less than 1%.

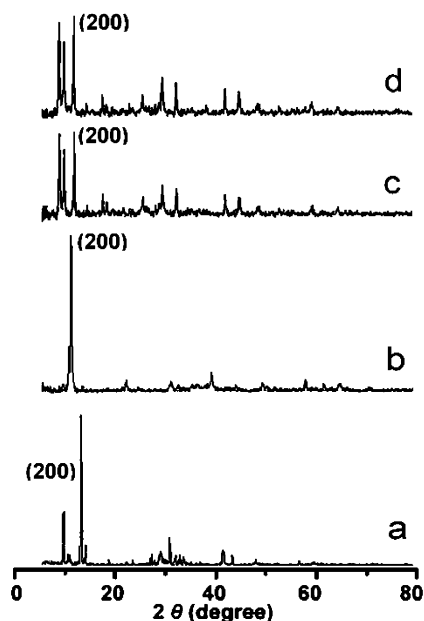


Figure 1. X-ray diffraction patterns of the following: (a) sample A, $\text{K}_2\text{Ti}_4\text{O}_9$ fibers; (b) sample B, $\text{H}_2\text{Ti}_4\text{O}_9 \cdot 1.2\text{H}_2\text{O}$ fibers; (c) sample C, $(\text{H}_3\text{O})_{0.5}\text{H}_{1.5}\text{Ti}_8\text{O}_{17} \cdot \text{H}_2\text{O}$ fibers; and (d) sample D, $(\text{H}_3\text{O})_{0.5}\text{H}_{1.5}\text{Ti}_8\text{O}_{17} \cdot \text{H}_2\text{O}$ fibers.

Figure 1a shows that the sample A is mainly $\text{K}_2\text{Ti}_4\text{O}_9$. In addition, K_2O -rich amorphous melt also uniformly disperses in the $\text{K}_2\text{Ti}_4\text{O}_9$ fibers because of continuous and uniform reactions between amorphous titania and potassium oxide starting from a low temperature.^{33–35} After the K_2O -rich amorphous melt is dissolved during the $\text{H}_3\text{O}^+/\text{K}^+$ exchange of $\text{K}_2\text{Ti}_4\text{O}_9$, voids appear at places of K_2O -rich melt and the interlayer K^+ of crystal structure. These voids give large BET surface area of $119.0 \text{ m}^2 \cdot \text{g}^{-1}$ and micropore surface area of $90.3 \text{ m}^2 \cdot \text{g}^{-1}$ for the ion-exchange product of $\text{H}_2\text{Ti}_4\text{O}_9 \cdot 1.2\text{H}_2\text{O}$ of sample B (see Table 1). Both micropores with diameters of $<1 \text{ nm}$ and mesopores with diameters of $1\text{--}4$ and $20\text{--}40 \text{ nm}$ are created in the crystalline $\text{H}_2\text{Ti}_4\text{O}_9 \cdot 1.2\text{H}_2\text{O}$ (see Table 1).

The $(\text{H}_3\text{O})_{0.5}\text{H}_{1.5}\text{Ti}_8\text{O}_{17} \cdot \text{H}_2\text{O}$ of sample C and sample D were prepared from the $\text{H}_2\text{Ti}_4\text{O}_9 \cdot 1.2\text{H}_2\text{O}$ of sample B by thermal treatments in air and in glycerine, respectively. They have high crystallinities, indicated by their XRD patterns shown in Figure 1. They all maintain large BET surface areas over $100 \text{ m}^2 \cdot \text{g}^{-1}$ and combinational micro-mesopores including micropores with diameters of $<1 \text{ nm}$ and mesopores with diameters in main ranges of $1\text{--}4 \text{ nm}$ and $20\text{--}40 \text{ nm}$, as shown in Table 1 and Figure 2. In Figure 2, the present $(\text{H}_3\text{O})_{0.5}\text{H}_{1.5}\text{Ti}_8\text{O}_{17} \cdot \text{H}_2\text{O}$ of both sample C and sample D could be of type I and/or IV in the BDDT classification.³⁸ A remarkable adsorption at low relative pressures suggests the presence of micropores.³⁹ In addition, both hysteresis loops resemble H4 in the IUPAC classification, indicating the presence of open slit-shaped mesopores with wide bodies and narrow, short necks. The pore size distribution curves, the inset in Figure 2, were calculated by using the MP method and BJH method, respectively revealing micropores with diameter of $<1 \text{ nm}$ and mesopores with diameters of $1\text{--}4$ and $20\text{--}40 \text{ nm}$.

According to the reported similar crystal structures,^{40–42} the scheme of crystal structures for illustrating the formation of micropores in sample C and sample D is shown in Figure 3. The basic $[\text{Ti}_4\text{O}_9]^{2-}$ sheets in both $(\text{H}_3\text{O})_{0.5}\text{H}_{1.5}\text{Ti}_8\text{O}_{17} \cdot \text{H}_2\text{O}$ and $\text{H}_2\text{Ti}_4\text{O}_9 \cdot 1.2\text{H}_2\text{O}$ are the same. $\text{H}_2\text{Ti}_4\text{O}_9 \cdot 1.2\text{H}_2\text{O}$ is prepared from $\text{K}_2\text{Ti}_4\text{O}_9$ by $\text{H}_3\text{O}^+/\text{K}^+$ exchange. The (200) reflections of layered titanates can be used to calculate the interlayer distance of adjacent $[\text{Ti}_4\text{O}_9]^{2-}$ sheets. (200) reflections of $\text{K}_2\text{Ti}_4\text{O}_9$ of

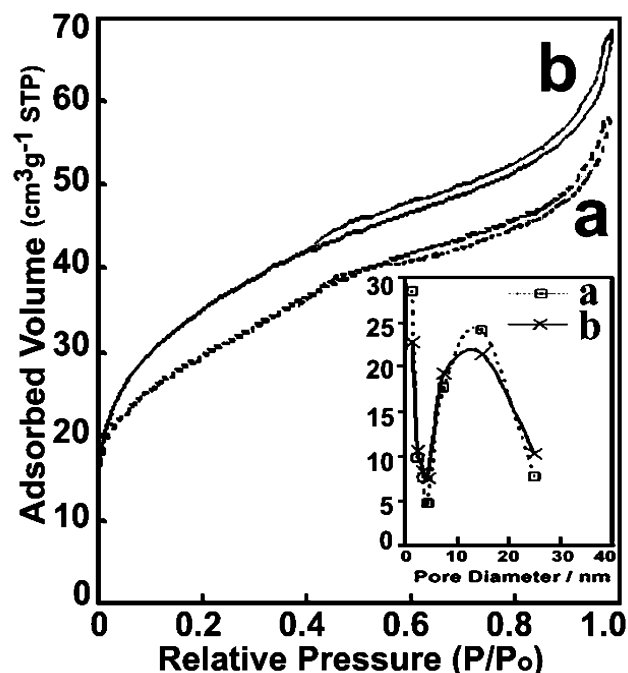


Figure 2. Nitrogen adsorption/desorption isotherms for (a) sample C and (b) sample D. Corresponding pore size distribution curves of (a) sample C and (b) sample D are shown in the inset.

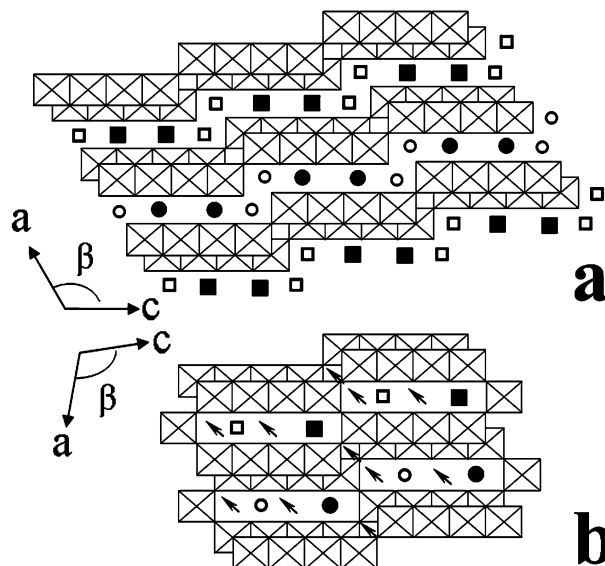


Figure 3. Idealized representation of crystal structures: (a) $\text{H}_2\text{Ti}_4\text{O}_9 \cdot 1.2\text{H}_2\text{O}$ projected along (010) and (b) $(\text{H}_3\text{O})_{0.5}\text{H}_{1.5}\text{Ti}_8\text{O}_{17} \cdot \text{H}_2\text{O}$ projected along (010). ● and ■, H_3O^+ ; ○ and □, H^+ ; ■ and □, H_3O^+ and H^+ at $y = 1/2$; ● and ○, H_3O^+ and H^+ at $y = 0$. The arrows represent the places of open voids and channels ($<1 \text{ nm}$) in the crystal structure.

sample A (Figure 1 a) and sample B (Figure 1b) indicate that $\text{H}_2\text{Ti}_4\text{O}_9 \cdot 1.2\text{H}_2\text{O}$ maintains the layered crystal structure (Figure 3a), nearly the same as that of $\text{K}_2\text{Ti}_4\text{O}_9$. Although the ionic radius of H^+ is smaller than the 1.38 \AA of K^+ , H^+ will combine with different amount of the additional hydrone, such as H_3O^+ with radius of 1.40 \AA , because of the ionic hydration.⁴⁵ As a result, the interlayer distance of the layered frameworks of $[\text{Ti}_4\text{O}_9]^{2-}$ sheets is enlarged from 8.70 \AA for $\text{K}_2\text{Ti}_4\text{O}_9$ to 8.93 \AA for $\text{H}_2\text{Ti}_4\text{O}_9 \cdot 1.2\text{H}_2\text{O}$. During the dehydration processing, the structure water in $\text{H}_2\text{Ti}_4\text{O}_9 \cdot 1.2\text{H}_2\text{O}$ is partly removed, and the $[\text{Ti}_4\text{O}_9]^{2-}$ sheets, each involving four octahedral TiO_6 units, shift by each other in the amount of $C/4$ in the structure of $\text{H}_2\text{Ti}_4\text{O}_9 \cdot 1.2\text{H}_2\text{O}$. They share free corners of four- TiO_6 units and

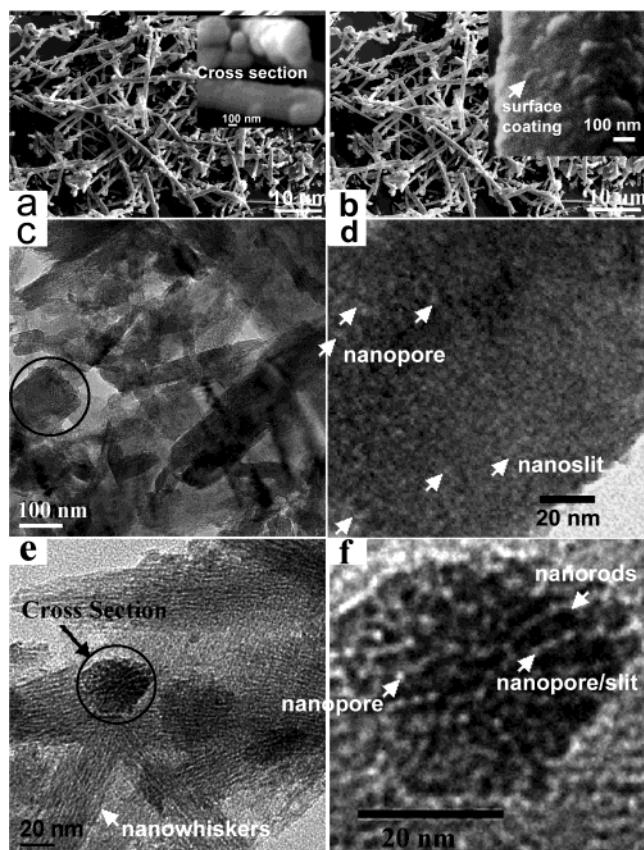


Figure 4. SEM micrographs of (a) sample C and (b) sample D.; Insets of (a) and (b) respectively show surface morphologies and structures at high magnification. Panels c and e, respectively, show representative HRTEM micrographs of sample C and sample D. Panels d and f, respectively, show the magnified side-view HRTEM micrograph of sample C and the cross-section-view HRTEM micrograph of sample D.

gradually condense each other to form tunnel-like crystal structure of $(\text{H}_3\text{O})_{0.5}\text{H}_{1.5}\text{Ti}_8\text{O}_{17}\cdot\text{H}_2\text{O}$, as shown in Figure 3b. Half the amount of oxygen located at the free corner of four- TiO_6 unit is removed by combining with the two H^+ located at the outside of four- TiO_6 unit to form the H_2O . As a result, the $(\text{H}_3\text{O})_{0.5}\text{H}_{1.5}\text{Ti}_8\text{O}_{17}\cdot\text{H}_2\text{O}$ contains H^+ , bound water, and crystal water. H^+ cannot enlarge the tunnel space due to its smaller radius, while the interlayer bound water of H_3O^+ acts as the pillaring agent to enlarge the tunnel space. They partly occupy and expand the tunnel space, which agrees with the interlayer distance expansion from reported 7.60 Å of $\text{H}_2\text{Ti}_8\text{O}_{17}$ to 7.96 Å, calculated from (200) reflections in XRD patterns shown in Figure 1c,d, of $(\text{H}_3\text{O})_{0.5}\text{H}_{1.5}\text{Ti}_8\text{O}_{17}\cdot\text{H}_2\text{O}$. Therefore, voids with sizes of <1 nm occur in the tunnel space of $(\text{H}_3\text{O})_{0.5}\text{H}_{1.5}\text{Ti}_8\text{O}_{17}\cdot\text{H}_2\text{O}$. Furthermore, channels with widths of <1 nm also exist at the corner-connected places of up and down basic $[\text{Ti}_4\text{O}_9]^{2-}$ sheets. These voids and channels, marked with arrow in Figure 3b, contribute to large surface area for micropores (<1 nm) within the $(\text{H}_3\text{O})_{0.5}\text{H}_{1.5}\text{Ti}_8\text{O}_{17}\cdot\text{H}_2\text{O}$ fibers. This agrees with the remarkable adsorptions at relatively low pressures, indicating the existence of micropores, of Figure 2.

The mesopores, together with morphologies and mesostructures, of sample C and sample D, are observed by SEM and HRTEM. The $(\text{H}_3\text{O})_{0.5}\text{H}_{1.5}\text{Ti}_8\text{O}_{17}\cdot\text{H}_2\text{O}$ of both sample C and sample D are fibers with diameters of 0.5–1.5 μm and lengths of 10–20 μm , as shown in Figure 4a,b. A SEM micrograph at high magnification (the inset of Figure 4a) shows that the $(\text{H}_3\text{O})_{0.5}\text{H}_{1.5}\text{Ti}_8\text{O}_{17}\cdot\text{H}_2\text{O}$ fibers prepared by the thermal treatment in air are nanoparticle agglomerates with clean surface. How-

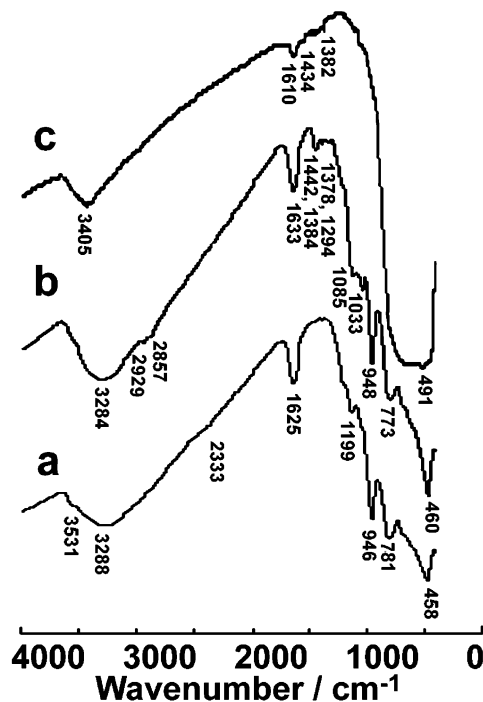


Figure 5. TF-IR vacuum spectra of (a) sample C, (b) sample D, and (c) P-25.

ever, for the $(\text{H}_3\text{O})_{0.5}\text{H}_{1.5}\text{Ti}_8\text{O}_{17}\cdot\text{H}_2\text{O}$ fibers prepared by the thermal treatment in glycerine, some surface coating is observed (the inset of Figure 4b). HRTEM micrographs of sample C (Figure 4c) and sample D (Figure 4e) both indicate that the $(\text{H}_3\text{O})_{0.5}\text{H}_{1.5}\text{Ti}_8\text{O}_{17}\cdot\text{H}_2\text{O}$ fibers consist of nanowhiskers with average diameter of ~ 30 nm and lengths up to 500 nm. Panels d and f, respectively, of Figure 4 show the magnified side-view HRTEM micrograph of sample C and the cross-section-view HRTEM micrograph of sample D, indicating that the $(\text{H}_3\text{O})_{0.5}\text{H}_{1.5}\text{Ti}_8\text{O}_{17}\cdot\text{H}_2\text{O}$ nanowhiskers are the agglomerate of nanorods with average diameter of ~ 3 nm and lengths of 5–10 nm. Nanopores with diameters of 1–4 nm and nanoslits with widths of 1–2 nm and lengths up to 8 nm are also observed within them. This agrees with the appearance of hysteresis loops in Figure 2, indicating the presence of open slit-shaped mesopores with wide bodies and narrow, short necks. As a result, $(\text{H}_3\text{O})_{0.5}\text{H}_{1.5}\text{Ti}_8\text{O}_{17}\cdot\text{H}_2\text{O}$ is combinational micro-mesoporous fibers.

Figure 5 shows the FTIR spectra of sample C and sample D in the frequency range of 400–4000 cm^{-1} , using P-25 as the standard sample for comparison. These spectra show the band of <500 cm^{-1} , due to the Ti–O stretching in TiO_6 octahedra. Meanwhile, an additional band around 780 cm^{-1} is observed in the spectra of samples C and D, which is subjected to the titania matrix of $[\text{Ti}_4\text{O}_9]^{2-}$ sheets. In addition, these spectra all show one broad band around 3400 cm^{-1} and one narrow band around 1630 cm^{-1} , while the Ti–OH bonding has bands around 3563, 3127, and 1600 cm^{-1} , and smaller crystallites could result in the broadness of the peaks.⁴⁶ Therefore, the observed peaks around 3400 and 1630 cm^{-1} correspond to the hydroxyl groups (O–H stretching) and surface adsorbed water (H–O–H bending). The peak intensity of these bands around 3400 and 1630 cm^{-1} are the same for sample C and sample D but become weaker for P-25, indicating a decreasing amount of surface adsorbed water and hydroxyl groups. This is due to the absence of hydronium ions and protons in the nonporous crystal structure of P-25. Bands around 950 cm^{-1} for sample C and sample D are assigned to H–O–H bending and O–H bending, indicating the existence of hydronium ions and protons in their crystal structure (Figure 3b). For sample D, additional absorptions

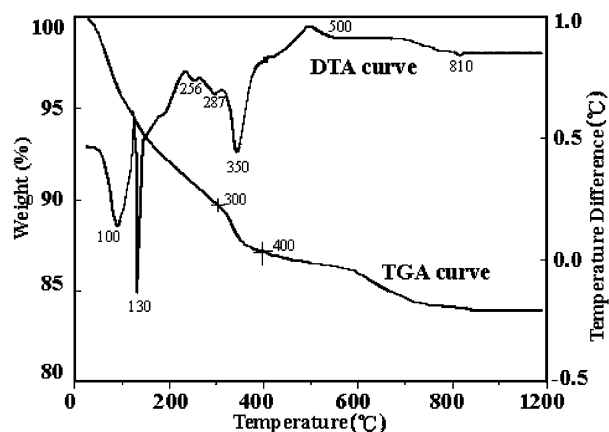


Figure 6. TGA-DTA profiles of sample B, $\text{H}_2\text{Ti}_4\text{O}_9 \cdot 1.2\text{H}_2\text{O}$ fibers.

around 1100, 1400, and 2900 cm^{-1} are assignable to stretching and bending vibrations of C–O vibration, $-\text{CH}_2-$ vibration, and $-\text{CH}_3$ stretching of alkyl groups, respectively, indicating the additional adsorbed glycerine with multi-OH groups. For photocatalytic reactions, the surface adsorbed water and hydroxyl groups are crucial. They will react with photoexcited holes on the catalyst surface and produce hydroxyl radicals, which is a powerful oxidant in degrading organics in water.⁴⁷ For solid acid catalysis, these $[\text{Ti}_4\text{O}_9]^{2-}$ sheets of the $(\text{H}_3\text{O})_{0.5}\text{H}_{1.5}\text{Ti}_8\text{O}_{17} \cdot \text{H}_2\text{O}$ are regarded as two-dimensional macropolyanions, which have been known to exhibit strong Brønsted and Lewis acidity when the counteranions are protons.^{30,48}

The thermal stability of the sample was investigated by TGA-DAT, as shown in Figure 6. The TGA curve exhibits a total weight loss of 16% for sample B of layered fibrous $\text{H}_2\text{Ti}_4\text{O}_9 \cdot 1.2\text{H}_2\text{O}$. A first 3.6% weight loss due to the rapid decrease of free water occurs below 100 °C and corresponds to an obvious endothermic peak at 100 °C on the DTA curve. The second 4.5% weight loss at 100–200 °C is due to the generation of $(\text{H}_3\text{O})_{0.5}\text{H}_{1.5}\text{Ti}_8\text{O}_{17} \cdot \text{H}_2\text{O}$ and corresponds to a strong sharp endothermic peak centered at 130 °C on the DTA curve. The endothermic peak at 130 °C is due to the generation of hydrous $(\text{H}_3\text{O})_{0.5}\text{H}_{1.5}\text{Ti}_8\text{O}_{17} \cdot \text{H}_2\text{O}$. There is around 4% weight loss at 200–400 °C, corresponding to three endothermic peaks on the DTA curve. Two smaller endothermic peaks at 200–300 °C are attributed to the structure transformation from $(\text{H}_3\text{O})_{0.5}\text{H}_{1.5}\text{Ti}_8\text{O}_{17} \cdot \text{H}_2\text{O}$ to $(\text{H}_3\text{O})_{0.5}\text{H}_{1.5}\text{Ti}_8\text{O}_{17}$. The large endothermic peak at 350 °C is attributed to crystallization of anhydrous $\text{H}_2\text{Ti}_8\text{O}_{17}$ which is stable at $T < 400$ °C.

From above, a scheme for the representation of the textural and surface properties of combinational micro-mesoporous titanate fibers is proposed and shown in Figure 7. During the calcination synthesis of $\text{K}_2\text{Ti}_4\text{O}_9$, four octahedral TiO_6 arrange side-by-side to form a $[\text{Ti}_4\text{O}_9]^{2-}$ nanosheet. Two to four layers of $[\text{Ti}_4\text{O}_9]^{2-}$ nanosheets are organized with interlayer K^+ to form the $\text{K}_2\text{Ti}_4\text{O}_9$ nanorods, with average diameters of 3 nm and lengths ranging from 5 to 10 nm, as shown in Figure 4d,f. Soluble K_2O -rich melt also generates and plays as a key role for creating mesoporous structures during the ion exchange reaction.^{34–36} In calcination, the K_2O -riched melt generates simultaneously and mixes with the $\text{K}_2\text{Ti}_4\text{O}_9$ nanorods to form nanowhiskers, with average diameter of 30 nm and lengths up to 500 nm, as shown in Figure 4c,e. These nanowhiskers also organize with K_2O -rich melt to form fibers, with diameters in range of 0.5–1.5 μm and lengths in range of 10–20 μm , as shown in Figure 4a,b. During the ion exchange reaction in acidic solution, the $\text{K}_2\text{Ti}_4\text{O}_9$ nanorods convert to layered $\text{H}_2\text{Ti}_4\text{O}_9 \cdot 1.2\text{H}_2\text{O}$ fibers with the layered crystal structure, as shown in Figure 3a. Subsequently solvothermal treatment of $\text{H}_2\text{Ti}_4\text{O}_9 \cdot$

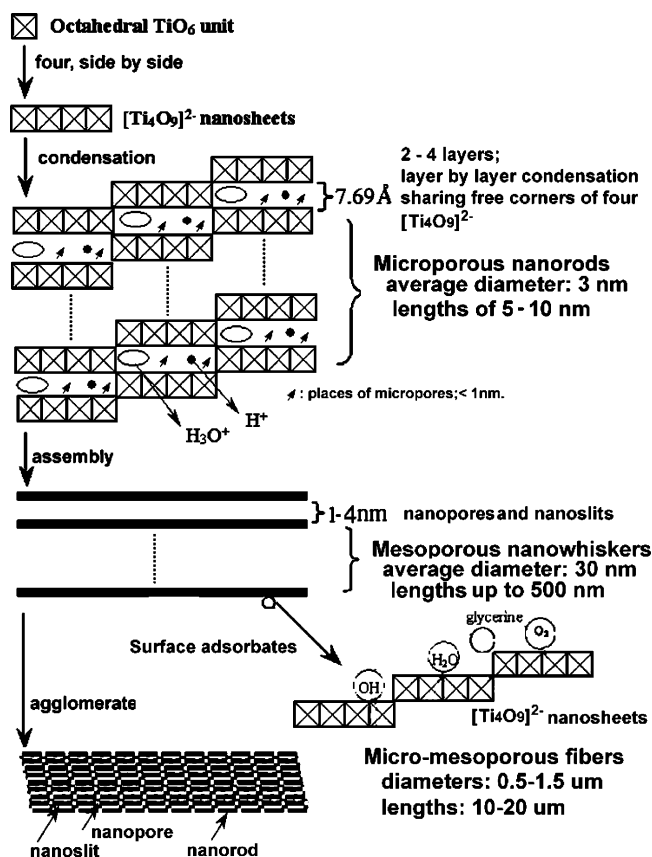


Figure 7. A bottom-up schematic representation of textural and surface properties of combinational micro-mesoporous octatitanate fibers.

$1.2\text{H}_2\text{O}$ results in condensation of $[\text{Ti}_4\text{O}_9]^{2-}$ nanosheets by which $(\text{H}_3\text{O})_{0.5}\text{H}_{1.5}\text{Ti}_8\text{O}_{17} \cdot \text{H}_2\text{O}$ nanorods with tunnel-like crystal structure, as shown in Figure 3b and Figure 7 are formed. Because of the part remove of water molecules in crystal structure, micropores, marked with arrows shown in Figure 3b and Figure 7, are generated. In addition to the ion exchange reaction, K_2O -rich melt organized with the $\text{K}_2\text{Ti}_4\text{O}_9$ nanorods in nanowhiskers and with nanowhiskers in fibers also dissolves to leave mesoporous structures within the nanowhiskers and fibers as shown Figure 7. The nanopores and nanorods in the present octatitanate fibers are low ordered. Further modified calcination synthesis of composites of K_2O -rich melt and potassium titanate, appropriate thermal treatments, and the use of surfactant can be adopted in order to prepare titanate and titania fibers with highly ordered porous structures and to further improve the catalytic activity. These works have been started and we have prepared relatively ordered titania fibers with surface area over $100 \text{ m}^2 \cdot \text{g}^{-1}$ from mixed potassium titanates by ion exchange reaction and thermal treatments. The crystal phase such as anatase, rutile, brookite and their mixed phase can be controlled.

3.2. Catalytic Activities of Combinational Micro-Mesoporous Octatitanate Fibers.

3.2.1. Photocatalytic Activities of Combinational Micro-Mesoporous Octatitanate Fibers. The time course of the photodegradation of methyl orange on UV light irradiated catalysts is shown in Figure 8. The kinetics of methyl orange discoloration over different samples was studied, which allows us to quantitatively know the effects of different catalysts on the apparent reaction rate constant. However, it should be strongly pointed out that the kinetics here only means apparent reaction kinetics because several processes contribute to the overall discoloration of methyl orange. Nevertheless, methyl orange has been used as a reliable model azo dye pollutant in

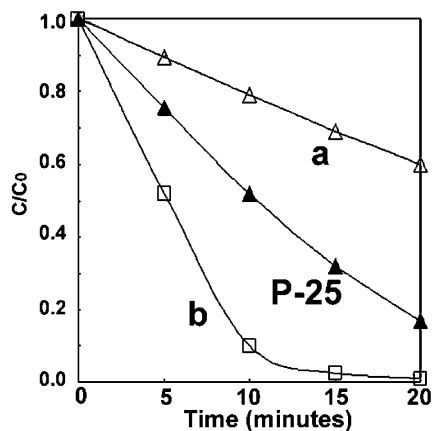


Figure 8. Photodegradation of methyl orange over (a) sample C, (b) sample D, and P-25.

photocatalytic research. Its discoloration, mineralization, and decomposition of methyl orange over P-25 have been studied well.^{49,50} Therefore, our experiments of using methyl orange as a model azo dye pollutant and P-25 as the standard sample can accurately evaluate photocatalytic activities of our samples. The kinetics of discoloration of methyl orange in water is described according to the pseudo-first-order equation as given below:

$$r = -\frac{dC}{dt} = k_a C \quad (1)$$

where r is the reaction rate, C is the concentration of methyl orange in water, t is the reaction time, and k_a is the pseudo-first-order rate constant.

On the basis of the data in the first 10 min presented in Figures 7, by plotting $\ln(C_0/C)$ as a function of time t , through regression, we obtained the k (min^{-1}) constants from the slope of the straight line for different samples. It should be pointed out that the choice of the data in the first 10 min lies in the fact that the data after 10 min significantly deviate from the straight line. This linear relation obeys the first-order reaction law that can be expressed by

$$\ln(C_0/C) = kt \quad (2)$$

where C_0 ($\text{mg}\cdot\text{L}^{-1}$), C ($\text{mg}\cdot\text{L}^{-1}$), and k (min^{-1}) are the methyl orange initial concentration, the residual concentration at the reaction time t , and the first-order rate constant, respectively. A higher k value means that this catalyst has higher activity for photodegradation of methyl orange. Regression results are given as the rising sequence of k with sample C, sample D, and P-25, as well as D (0.236) > P-25 (0.065) > C (0.019). This indicates that photooxidative activities of all samples are directly related to their textural and surface properties. P-25, a mixture of anatase and rutile, is one of the active standard photocatalysts. Both sample C and sample D are $(\text{H}_3\text{O})_{0.5}\text{H}_{1.5}\text{Ti}_8\text{O}_{17}\cdot\text{H}_2\text{O}$ fibers consisting of tunnel-like arrangements of $[\text{Ti}_4\text{O}_9]^{2-}$ sheets. They have very large surface area over $100 \text{ m}^2\cdot\text{g}^{-1}$ among examined samples. Surface hydroxylation modification is done for sample D by the thermal treatment in glycerine.

Photooxidative activities of all samples have direct relation to their material structures and the surface modification. The $(\text{H}_3\text{O})_{0.5}\text{H}_{1.5}\text{Ti}_8\text{O}_{17}\cdot\text{H}_2\text{O}$ of sample C and sample D have basic tunnel crystal structure, as shown in Figure 3b. Open voids (<1 nm) existing in half part of tunnel space and opened channel-like voids existing at the corner-connected places of up and down basic $[\text{Ti}_4\text{O}_9]^{2-}$ sheets contribute to large surface area of micropores (<1 nm). In addition, the octatitanate fibers consist

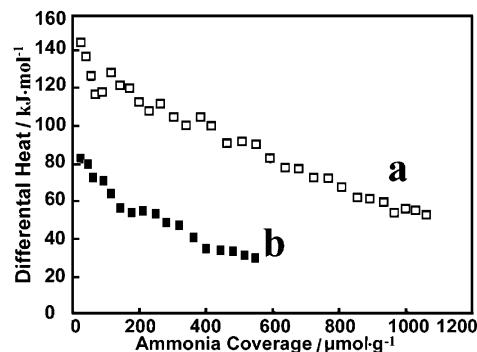


Figure 9. Differential heat versus coverage for NH_3 adsorption on surface acidity of combinational micro-mesoporous octatitanate fibers of (a) sample C and (b) sample D.

of nanowhiskers containing mesoscopic nanoslits and nanorods. Therefore, a large surface area increases the available surface active sites and leads to a higher photonic efficiency from a higher interfacial charge carrier transfer rate. However, all of charge carriers (e^-/h^+ pairs) generated in the basic four- TiO_6 octahedra are close to surface of $[\text{Ti}_4\text{O}_9]^{2-}$ nanosheets and quickly move to the nanorod surface. They undergo rapid surface recombination mainly due to abundant surface trapping sites and the lack of driving force for e^-/h^+ pair separation. For sample C, although a certain amount of e^-/h^+ pairs react with the preadsorbed hydroxyl OH, H_2O , and O_2 to form active $\text{OH}\cdot$ free radicals, $\text{O}_2^{\cdot-}$, $\text{O}\cdot\text{OH}$, the time for the e^-/h^+ surface charge carrier recombination is still much shorter than that of the interfacial charge transfer, due to very fine nanorods with diameters of <3 nm similar to that of very smaller nanocrystals. Its photocatalytic activity, therefore, is low. This agrees with the phenomenon that there is the optimal size for titania nanocrystals with the highest activity.^{11,51} As a result, the maximum photocatalytic efficiency of nanoporous titanates can be attained by accelerating the interfacial charge carrier transfer and charge carrier trapping.

Glycerine is a weak polarity solvent with multihydroxyls and a boiling point of near 300°C . The stable structure transformation from $\text{H}_2\text{Ti}_4\text{O}_9\cdot 1.2\text{H}_2\text{O}$ to $(\text{H}_3\text{O})_{0.5}\text{H}_{1.5}\text{Ti}_8\text{O}_{17}\cdot\text{H}_2\text{O}$ processes from the fiber surface to the fiber inner body in glycerine at 250°C . The glycerine also adsorbs in the mesopores of octatitanate fibers of sample D, providing much more adsorbed hydroxyls that accelerate the interfacial charge transfer. Further, the large size of $(\text{H}_3\text{O})_{0.5}\text{H}_{1.5}\text{Ti}_8\text{O}_{17}\cdot\text{H}_2\text{O}$ fibers can decrease the mass-transfer limitation on the fiber surface, which make it possible for much more methyl orange molecules to easily diffuse from the solution body to the fiber surface. Mesopores with diameters of 1–4 and 20–40 nm within titanate fibers are large enough to accommodate large amount of adsorbed methyl orange.⁵² Therefore, the amount of methyl orange adsorbed on the surface of nanoporous octatitanate is not the controlling factor. As a result, the highly photocatalytic efficiency of sample D is due to the accelerated interfacial charge transfer and charge carrier trapping through the surface modification with adsorbed glycerine molecules.

3.2.2. Acidities of Combinational Micro-Mesoporous Octatitanate Fibers. Microcalorimetric adsorption of NH_3 was used to determine the number and strength of surface acid sites on the catalysts and the results are shown in Figure 9. The nanoporous titanate fibers of sample C exhibit the strongest acidity with an initial heat of $145 \text{ kJ}\cdot\text{mol}^{-1}$ and coverage of $1100 \mu\text{mol}\cdot\text{g}^{-1}$ for the adsorption of NH_3 , as shown in Figure 9a. However, the nanoporous titanate fibers of sample D exhibit the relatively low acidity with an initial heat of $85 \text{ kJ}\cdot\text{mol}^{-1}$

and coverage of $480 \mu\text{mol}\cdot\text{g}^{-1}$ for the adsorption of NH_3 as shown in Figure 9b.

It has been reported that H^+ -exchanged layered compounds have both Brønsted and Lewis acidity.^{48,53} For layered transition-metal oxides such as titanates, application in solid acid catalysis has not been investigated because of the difficulty of the intercalation of reactant molecules due to the high charge density of the nanosheets such as the $[\text{Ti}_4\text{O}_9]^{2-}$ nanosheets.^{54–57} Although the exfoliation of the layered nanosheets has been proposed as an alternative way to overcome this disadvantage and provide the strong Brønsted acidity, they cannot be produced in large scale with low cost. The present combinational micro-mesoporous $(\text{H}_3\text{O})_{0.5}\text{H}_{1.5}\text{Ti}_8\text{O}_{17}\cdot\text{H}_2\text{O}$ fibers have similar H^+ -exchanged crystal structure containing micropores with large surface, exhibiting strong acidity due to large amount of intercalated protons and hydrate protons in crystal structure. Their basic structure units of nanorods share similar size with those of reported exfoliated nanosheets. The bulk size is also similar to those of aggregated nanosheets. Additional mesoporous channels between the adjacent titanate nanorods are large enough to intercalate the large reactant and product molecules. The modification or loading can also be done on them. Therefore, it is possible for the present combinational micro-mesoporous $(\text{H}_3\text{O})_{0.5}\text{H}_{1.5}\text{Ti}_8\text{O}_{17}\cdot\text{H}_2\text{O}$ fibers to be used for solid acid catalyst and catalyst support.

4. Conclusions

Novel combinational micro-mesoporous $(\text{H}_3\text{O})_{0.5}\text{H}_{1.5}\text{Ti}_8\text{O}_{17}\cdot\text{H}_2\text{O}$ fibers were prepared by thermal treatments of layered protonic tertatitanate fibers both in glycerine and in air. Nanostructures of nanowhiskers, nanorods, nanoslits, micropores, and mesopores coexist in the titanate fibers, contributing to both large surface area and multi-scale interconnected nanopore channels. The presence of a combinational pore distribution is considered advantageous, as micropores and intercalated protons, respectively, provide titanate fibers with large surface area and very strong surface acidity, while mesopores are responsible for a fast mass transport for reactants and products. The solvothermal reaction in glycerine gives a mild reaction condition for preparing active octatitanate fibers. The reason for the excellent catalytic activities in photocatalysis and solid acid catalysis lies in their distinguished textural and surface properties. The obtained protonic octatitanate fibers with novel combinational micro-mesoporous structures show potential application in both photocatalysis and solid acid catalysis.

Acknowledgment. The authors appreciate Professor J. Shen of Department of Chemistry, Nanjing University, China, for the microcalorimetric measurements and discussion.

References and Notes

- (1) Corma, A.; Garcia, H. *Chem. Rev.* **2002**, 102(10), 3837.
- (2) Linsebigler, A. L.; Lu, G. Q.; Yates, J. T. Jr. *Chem. Rev.* **1995**, 95(3), 735.
- (3) Hu, S.; Willey, R. J.; Notari, B. J. *Catal.* **2003**, 220, 240.
- (4) Ding, Z.; Lu, G. Q.; Greenfield, P. F. *J. Phys. Chem. B* **2000**, 104, 4815.
- (5) Hirakawa, T.; Kominami, H.; Ohtani, B.; Nosaka, Y. *J. Phys. Chem. B* **2001**, 105, 6993.
- (6) Davis, M. E. *Nature* **2002**, 417, 813.
- (7) Andersson, M.; Osterlund, L.; Ljungstrom, S.; Palmqvist, A. *J. Phys. Chem. B* **2002**, 106 (41), 10674.
- (8) Lee, W. G.; Woo, S. I.; Kim, J. C.; Choi, S. H.; Oh, K. H. *Thin Solid Films* **1994**, 237, 105.
- (9) Trentler, T. J.; Denler, T. E.; Bertone, J. F.; Agrawal, A.; Colvin, V. L. *J. Am. Chem. Soc.* **1999**, 121, 1613.
- (10) Wong, J. C. S.; Linsebigler, A.; Lu, G.; Fan, J.; Yates, J. T., Jr. *J. Phys. Chem.* **1995**, 99, 335.
- (11) Zhang, Z.; Wang, C.; Zakaria, R.; Ying, J. Y. *J. Phys. Chem. B* **1998**, 102, 10871.
- (12) Horikoshi, S.; Saitou, A.; Hidaka, H.; Serpone, N. *Environ. Sci. Technol.* **2003**, 37, 5813.
- (13) Al-Ekabi, H.; Serpone, N. *J. Phys. Chem.* **1988**, 92, 5726.
- (14) Gates, B. C. *Chem. Rev.* **1995**, 95 (3), 511.
- (15) Clark, J. H.; Rhodes, C. N., Eds. In *Clean Synthesis Using Porous Inorganic Solid Catalysts and Supported Reagents*; Royal Society of Chemistry: Cambridge, 2000.
- (16) Fox, M. A.; Dulay, M. T. *Chem. Rev.* **1993**, 93, 341.
- (17) Peill, N. J.; Hoffmann, M. R. *Environ. Sci. Technol.* **1995**, 29, 2974.
- (18) Peill, N. J.; Hoffmann, M. R. *Environ. Sci. Technol.* **1996**, 30, 2806.
- (19) Corma, A. *Chem. Rev.* **1997**, 97(6), 2373.
- (20) Soler-Illia, G. J. de A. A.; Sanchez, C.; Lebeau, B.; Patarin, J. *Chem. Rev.* **2002**, 102 (11), 4093.
- (21) Ying, J. Y.; Mehnert, C. P.; Wong, M. S. *Angew. Chem., Int. Ed. Engl.* **1999**, 38, 56.
- (22) Yang, P.; Zhao, D.; Margolese, D. I.; Chmelka, B. F.; Stucky, G. D. *Nature* **1998**, 396, 152.
- (23) Katou, T.; Lee, B.; Lu, D.; Kondo, J. N.; Hara, M.; Domen, K. *Angew. Chem., Int. Ed. Engl.* **2003**, 42, 2382.
- (24) Lee, B.; Lu, D.; Kondo, J. N.; Domen, K. *J. Am. Chem. Soc.* **2002**, 124, 11256.
- (25) Crepaldi, E. L.; Soler-Illia, G. J. de A. A.; Grosso, D.; Cagnol, F.; Ribot, F.; Sanchez, C. *J. Am. Chem. Soc.* **2003**, 125, 9970.
- (26) Clearfield, A. *Chem. Rev.* **1988**, 88, 125.
- (27) Han, Y. S.; Choy, J. H. *J. Mater. Chem.* **1998**, 8, 1459.
- (28) Shangguan, W.; Yoshida, A. *J. Phys. Chem. B* **2002**, 106, 12227.
- (29) Yin, S.; Sato, T. *Ind. Eng. Chem. Res.* **2000**, 39, 4526.
- (30) Takagaki, A.; Sugisawa, M.; Lu, D.; Kondo, J. N.; M. Hara; Domen, K.; Hayashi, S. *J. Am. Chem. Soc.* **2003**, 125, 5479.
- (31) Sasaki, T.; Izumi, F.; Watanabe, M. *Chem. Mater.* **1996**, 8, 777.
- (32) Bao, N.; Lu, X.; Ji, X.; Feng, X.; Xie, J. *Fluid Phase Equilibria* **2002**, 193, 229.
- (33) Bao, N.; Feng, X.; Shen, L.; Lu, X. *Cryst. Growth Des.* **2002**, 2 (5), 437.
- (34) Bao, N.; Shen, L.; Feng, X.; Lu, X. *J. Am. Ceram. Soc.* **2004**, 87 (3), 326.
- (35) Bao, N.; Feng, X.; Shen, L.; Lu, X.; Yanagisawa, K. *AIChE J.* **2004**, 50 (7), 1568.
- (36) Bao, N.; Feng, X.; Yang, Z.; Shen, L.; Lu, X. *Environ. Sci. Technol.* **2004**, 38, 2729.
- (37) Andersson, M.; Osterlund, L.; Ljungstrom, S.; Palmqvist, A. *J. Phys. Chem. B* **2002**, 106 (41), 10674.
- (38) Choy, J. H.; Lee, H. C.; Jung, H.; Kim, H.; Boo, H. *Chem. Mater.* **2002**, 14, 2486.
- (39) Ide, Y.; Ogawa, M. *Chem. Commun.* **2003**, 1262.
- (40) Sasaki, T.; Watanabe, M.; Fujiki, Y.; Kitami, Y. *Chem. Mater.* **1994**, 6, 1749.
- (41) Sasaki, T.; Watanabe, M.; Komatsu, Y.; Fujiki, Y. *Inorg. Chem.* **1985**, 24, 2265.
- (42) Izawa, H.; Kikkawa, S.; Koizumi, M. *J. Phys. Chem.* **1982**, 86, 5023.
- (43) Alnuncourt, R. N.; Kurtz, M.; Wilmer, H.; Löffler, E.; Hagen, V.; Shen, J.; Muhler, M. *J. Catal.* **2003**, 220, 249.
- (44) Gregg, S. J.; Sing, K. S. W., Eds. In *Adsorption, Surface Area and Porosity*; Academic Press: London, 1982.
- (45) Clearfield, A. *Inorganic Ion Exchange Materials*; CRC Press: Boca Raton, FL, 1982.
- (46) Henderson, M. A.; Epling, W. S.; Peden, C. H. F.; Perkins, C. L. *J. Phys. Chem. B* **2003**, 107, 534.
- (47) Joseph, J. M.; Destailhats, H.; Hung, H.-M.; Hoffmann, M. R. *J. Phys. Chem. A* **2000**, 104, 301.
- (48) Mizuno, N.; Misono, M. *Chem. Rev.* **1998**, 98, 199.
- (49) Cornu, C. J. G.; Colussi, A. J.; Hoffmann, M. R. *J. Phys. Chem. B* **2003**, 107, 3156.
- (50) Almquist, C. B.; Biswas, P. *J. Catal.* **2002**, 212, 145.
- (51) Maira, A. J.; Yeung, K. L.; Lee, C. Y.; Yue, P. L.; Chan, C. K. *J. Catal.* **2000**, 192, 185.
- (52) Costantino, U.; Coletti, N.; Nocchetti, M.; Aloisi, G. G.; Elisei, F. *Langmuir* **1999**, 15, 4454.
- (53) Sasaki, T.; Watanabe, M. *J. Am. Chem. Soc.* **1998**, 120, 4682.
- (54) Sasaki, T.; Nakano, S.; Yamauchi, S.; Watanabe, M. *Chem. Mater.* **1997**, 9, 602.
- (55) Yagi, M.; Kaneko, M. *Chem. Rev.* **2001**, 101, 21.
- (56) Hou, W.; Yan, Q.; Peng, B.; Fu, X. *J. Mater. Chem.* **1995**, 5, 109.
- (57) Ohya, T.; Nakayama, A.; Ban, T.; Ohya, Y.; Takahashi, Y. *Chem. Mater.* **2002**, 14(7), 3082.